

MICRO-TERRAIN FEATURE EXTRACTION FROM NUMERICAL ANALYSIS OF GRIDDED LIDAR DATA

S. Bruce Blundell, Physical Scientist
U.S. Army ERDC Topographic Engineering Center
7701 Telegraph Road
Alexandria, VA 22315-3864
s.bruce.blundell@usace.army.mil

Randy Swanson, Geographer
U.S. Army Geospatial Center
7701 Telegraph Road
Alexandria, VA 22315-3864
randall.j.swanson@usace.army.mil

ABSTRACT

High-resolution digital elevation models (DEMs) created from small-footprint airborne Light Detection and Ranging (LIDAR) scanning system data contain information that can reveal micro-terrain features and their spatial patterns, especially in the absence of dense forest overstory. We applied numerical techniques to a bare-earth gridded LIDAR DEM of a region containing both coniferous canopy and open rugged terrain to calculate directed second derivatives for each matrix location by fitting cubic splines to the data. Thresholding the results allowed the creation of spatially correlated layers of (1) micro-terrain features identified by rapid slope change and (2) associated azimuthal directions of maximum slope change. Canopy layers were created from first and last return LIDAR grids using a thresholded differencing algorithm. These layers along with the first, last and bare-earth LIDAR grids were imported into a GIS framework for further analysis. Results showed that broad patterns and individual features such as scarp fields and gullies may be extracted and mapped from small-footprint LIDAR digital surface models using numerical methods. Additional analyses such as vertical profiling of micro-terrain features to show changes in slope and break-in-slope, spatial correlation of directional features, and off-road route finding can then be performed. These techniques may be applied to geological trend analysis, military mobility, and the mapping of small-scale erosional features.

Key Words: LIDAR, Numerical Methods, Cubic Splines, GIS, Micro-Terrain.

INTRODUCTION

The development of airborne LIDAR laser scanning technology systems has been successfully applied to terrain modeling and analysis, such as in determining forest structure (Watt and Donoghue, 2005), extracting urban features (Priestnall, et al., 2000), and in understanding dynamic coastal environments (Woolard and Colby, 2002; Mitasova, et al., 2005). With denser point spacing and higher laser pulse frequencies, LIDAR-derived maps have been produced showing sub-meter structure of the earth's surface with geodetic accuracy (Carter, et al., 2007).

Commercial airborne LIDAR remote sensing systems generate rapid laser infrared pulses from an aircraft platform to acquire sequential range measurements over the terrain, allowing the creation of surface models from the elevation values associated with the voluminous pulse returns recorded in a typical data collection mission. Pulse energy is highly reflective from surfaces encountered, enabling the derivation of range measurements from pulse travel times. These distances are then related to a geoid model from the absolute position and attitude of the aircraft to provide the geographic position and elevation of each pulse return. Airborne scanners can discriminate first return, last return, and often multiple returns from each pulse. In modern systems, pulse repetition rates have reached

DISTRIBUTION STATEMENT A – APPROVED FOR PUBLIC RELEASE; DISTRIBUTION IS UNLIMITED

150,000 per second, allowing typical pulse densities on the ground of greater than one return per square meter (Chen, 2007). Higher pulse densities can be achieved at lower altitudes or with multiple scans over the same area.

LIDAR pulse return positions are used to create a DEM of the surface. If the DEM is created from the first return reflective surface, it is known as a Digital Surface Model (DSM). In forested areas, the detection of multiple returns per laser pulse can provide for the extraction of canopy structure information due to the distribution of returned energy from the vertical profile of the canopy (Dubayah and Drake, 2000). Some of the energy may be returned from the below-canopy ground surface, making the extraction of a bare-earth DEM, or Digital Terrain Model (DTM) of the ground surface, feasible. Bare-earth algorithms also extract buildings as non-ground returns (Fowler, 2001).

To create DEMs from any or all LIDAR returns, the LIDAR point cloud data must be interpolated into a set of regular matrices or grids. To create a bare-earth DTM, either the point cloud data or the set of multiple-return matrices must be filtered into ground and non-ground returns in post-processing. This often involves morphological or slope-based filtering by considering the local attributes of individual points. Other approaches include the use of feature attributes based on the segmentation of groups of points (Lee, 2004) and the fusion of pulse intensity information with their elevation values (Hu and Tao, 2004).

The diameter of laser pulse footprints on the ground from airborne systems ranges from 5-30 centimeters (Dubayah and Drake, 2000). In spite of the high sampling rate and vertical accuracy of LIDAR systems, LIDAR pulse footprints are non-contiguous, resulting in undersampling of surface features. This represents a disadvantage for airborne LIDAR in the detection of breaklines. However, researchers have used LIDAR data to detect and map terrain features with discontinuous elevation characteristics, including channel profiles (Miller, et al., 2004); earthquake-induced trenches (Johnson, et al., 2004); and fault scarps (Engelkemir and Khan, 2008).

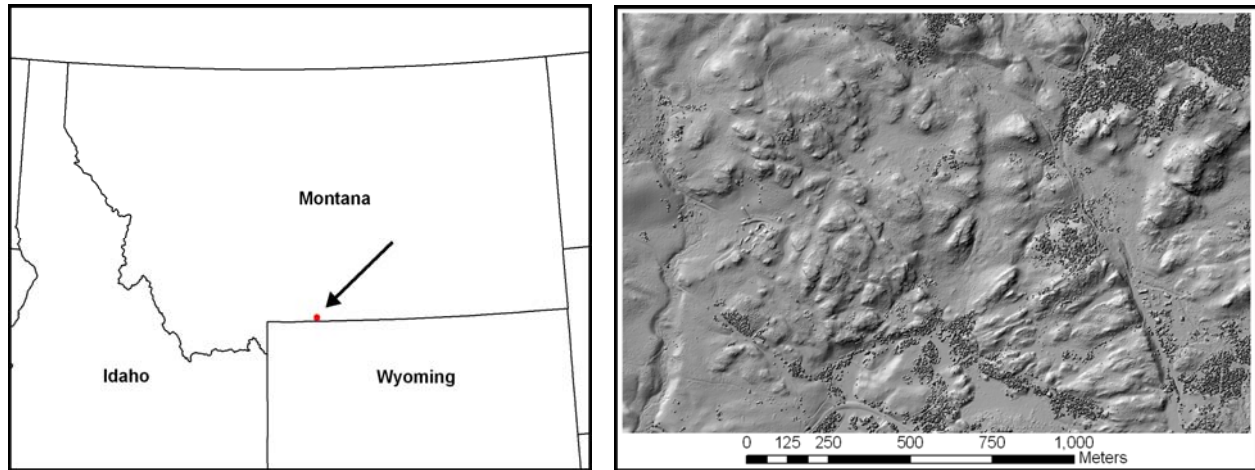
In this work, we investigate the use of spline-related numerical techniques applied to small-footprint gridded airborne LIDAR to detect micro-terrain surface features with vertical extent on the order of a few meters in the absence of dense forest overstory. Such features might include gullies, channels, small scarps, and boulder fields. We extract these features from a LIDAR-derived bare-earth DTM in order to map their spatial patterns, create vertical profiles of individual features, and perform route-finding analyses in combination with other extracted feature classes in a GIS environment.

DATA

The study site for this work is a 2.46 square kilometer area of high, open, rugged terrain with some canopy cover located in the Gallatin National Forest in southwestern Montana (Figure 1) along the border with Wyoming, approximately one kilometer to the northeast of Cooke City. Elevations are greater than 2400 meters above sea level. The surrounding region is influenced by the geology of the Yellowstone area, and is drained by streams following joints or cracks in the granitic bedrock (Fritz, 1994). Rugged highlands lie to the north, a region drained by tributaries of the Soda Butte Creek valley. Forest cover in this region is overwhelmingly represented by five coniferous species: subalpine fir, lodgepole pine, whitebark pine, Engelmann spruce, and Douglas fir (DeBlander, 2001). Yellowstone National Park lies beyond Cooke City to the south and west. Figure 2 shows a shaded relief image (North up) of the study site generated from the LIDAR first return DSM with canopy represented by darker, fine-grained texture. The LIDAR data has a ground sampling distance (GSD) of one meter with the study area comprising a matrix of 1920 x 1280 grid cells.

The LIDAR data was collected in the summer of 2003 and was provided by the U.S. Army Geospatial Center. The scanning system used was the Optech Airborne Laser Terrain Mapper (ALTM) mounted on a DeHavilland DHC-7 aircraft. The aircraft's position was continuously updated during flight with Global Positioning System (GPS) and inertial navigation system (INS) data feeds, resulting in absolute LIDAR positional accuracies of 0.5 m in the horizontal and 0.3 m in the vertical. The LIDAR first and last return grids were provided in 32-bit floating point GeoTIFF format and registered to the WGS-84 ellipsoid.

LIDAR Analyst from Visual Learning Systems, Inc. was used to create the bare-earth DTM from the first and last return DSM grids. The DTM was then input into the extraction process for generation of micro-terrain surface features. The first and last return DSM grids were also input into a differencing algorithm employed to create a canopy layer.



Figures 1 and 2. Study site location (left) and shaded relief from first return LIDAR DSM (right).

METHODOLOGY

This study involved the analysis and processing of LIDAR terrain elevation data within ITT Corporation's ENVI image processing environment for the extraction of micro-terrain breaklines as indicators of such features as channels, escarpments, gullies, and the surface expression of faults and joints due to differential erosion. An algorithm incorporating thresholded spline computations was developed in ENVI's Interactive Data Language (IDL) programming environment in order to capture breaklines in the bare-earth DTM as well as their directional trends. The distribution and extent of these features were mapped and elevation profiles of selected features were compared. Canopy areas were also extracted in IDL and the canopy and micro-terrain feature layers were imported into ESRI's ArcGIS environment for further analysis. Within ArcGIS, additional layers including terrain slope, roads, buildings, rivers, and streams were created and combined with the micro-terrain data as potential obstructive features in the application of off-road route-finding.

Canopy Extraction

To delineate canopy, a pulse differencing algorithm was developed to create an elevation difference grid from the first and last return DSM grids. The elevation difference grid contains some negative values as well as very small positive values that are not spatially correlated with canopy. A lower elevation difference threshold was chosen to exclude these non-canopy grid cells from the canopy layer. This lower threshold was found by examination of a histogram (not shown) of pulse return difference values. The histogram indicates a central spike with bins containing a large number of grid cells clustered around zero. In previous work (Blundell, 2006) it was found that a natural break point occurs in this dataset at the base of this spike that separates non-canopy from canopy difference grid cells. This lower elevation difference threshold was found to be 0.25 meters. Difference pixels above the threshold were saved as a canopy layer for analysis in ArcGIS.

Micro-Terrain Extraction

Processing of the bare-earth DTM effectively removed canopy areas that otherwise would have been extracted along with actual breaklines resulting from sudden changes in slope in the LIDAR-derived, fine-grained tree crown elevation textures. Algorithms were developed in IDL to rapidly characterize sudden elevation changes within the bare-earth DTM by calculating the directed second derivative, or Laplacian, for each grid cell. A numerical estimation is calculated of the unknown continuous function represented by successive elevation values along a line from the grid cell in a particular direction. This results in a set of Laplacian estimations for that grid cell, one for each of eight directions defined on the matrix. From these values the maximum absolute value of the Laplacian, its sign, and its associated direction are then saved in matrix array layers for each grid cell.

The methods used here for calculating the directed derivatives by numerical methods within a LIDAR gridded elevation model were developed during a previous effort to identify small-scale topographic breaklines as barriers to military mobility by the manual extraction and analysis of elevation profiles (Blundell, et al., 2004). That scheme

involved the identification of neighboring grid cells that define a set of eight directions emanating from an arbitrary central grid cell in a moving kernel window. Figure 3 depicts the grid cell identification process for an arbitrary elevation matrix location at the center of a 9x9 window.

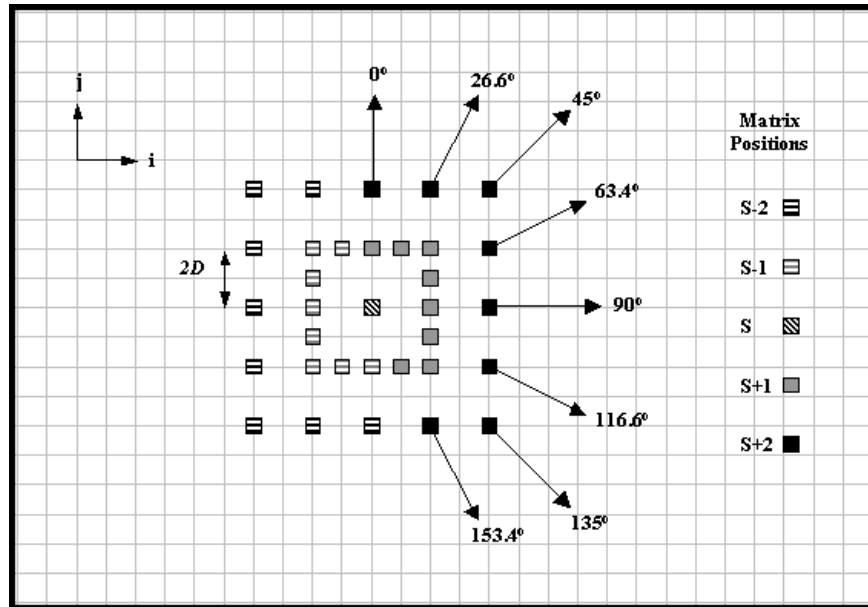


Figure 3. DSM matrix positions for numerical Laplacian calculation.

Matrix locations are shown for a series of eight directions between 0 and 180 degrees. The north or j direction in Figure 3 corresponds to 0 degrees. Laplacian value computations for the range 180 to 360 degrees are redundant and are not necessary. Ground distance between adjacent elevation matrix samples (ΔS) is a function of direction θ and the sensor ground sample distance D . For the 9x9 window shown in Figure 3, successive matrix positions S from the center grid cell are identified at every other DTM grid cell location in the i and j directions (distance $2D$). For eight directions, $2D$ is the minimum value for ΔS . Table 1 provides values for $\Delta S_{\theta}/D$, or the ground distance between successive S positions in a particular direction, normalized by ground sample distance, for chosen directions and computation window sizes. The gridded LIDAR data used in this work has a D value of one meter.

Table 1. $\Delta S_{\theta}/D$ Values by Direction (θ) and Window Size

θ	5x5	9x9	17x17	33x33
0°	1	2	4	8
$\tan^{-1} 1/2$	---	$\sqrt{5}$	$2\sqrt{5}$	$4\sqrt{5}$
45°	$\sqrt{2}$	$2\sqrt{2}$	$4\sqrt{2}$	$8\sqrt{2}$
$\tan^{-1} 2$	---	$\sqrt{5}$	$2\sqrt{5}$	$4\sqrt{5}$
90°	1	2	4	8
$\tan^{-1} -1/2$	---	$\sqrt{5}$	$2\sqrt{5}$	$4\sqrt{5}$
135°	$\sqrt{2}$	$2\sqrt{2}$	$4\sqrt{2}$	$8\sqrt{2}$
$\tan^{-1} -2$	---	$\sqrt{5}$	$2\sqrt{5}$	$4\sqrt{5}$

The scheme shown in Figure 3 avoids the need for interpolation between DTM elevation values. However, this limits the choices for window sizes when calculating for eight directions to 5x5, 9x9, 17x17, 33x33, 65x65, etc. In the IDL-based suite of algorithms developed for this work, the user chooses one of the above window sizes for processing. Window sizes greater than 33x33 were not used for analysis due to the reduced horizontal resolution of

calculated changes in slope associated with larger kernel window sizes. As shown in Table 1, the maximum absolute value of the Laplacian must be found from values calculated for only four directions in the case of the 5x5 window; the larger window sizes allow eight directions to be used.

Using this scheme, cubic spline interpolation was applied to a short sequence of five elevation points, including a central pixel, to generate the Laplacian values for each direction. For cubic splines, third-order connecting polynomials (not shown) are derived for each interval in the elevation point series, given assumptions about the function values and its derivatives at each point (Chapra and Canale, 2002). The polynomials contain the second derivatives at the ends of each interval. If they are then differentiated with the condition that the first derivatives at the interior points must be continuous, an expression results containing only derivatives of the second order. These derivatives can be evaluated by applying the expression to each interior point in the series in the following manner. For the five-point series $S-2$, $S-1$, S , $S+1$, and $S+2$ defined in a particular direction θ in Figure 3, an expression is formed for each of the three interior points, and appears as

$$E''_{S-1,\theta} + 4E''_{S,\theta} + E''_{S+1,\theta} = 6(E_{S+1,\theta} - 2E_{S,\theta} + E_{S-1,\theta}) / \Delta S_\theta^2 \quad (1)$$

where $E_{S,\theta}$ is the elevation value at matrix position $S = S(i,j)$ for which the Laplacian $E''_{S,\theta}$ is required in direction θ from position S . ΔS_θ is the ground distance between successive elevation matrix samples and is a function of θ and the sensor ground sample distance D . The quantities $E_{S+1,\theta}$ and $E_{S-1,\theta}$ are elevation values at matrix positions on either side of matrix position S associated with direction θ . Figure 4 depicts an example of an elevation profile from the LIDAR DTM with the series of five matrix positions $S-2$, $S-1$, S , $S+1$, and $S+2$.

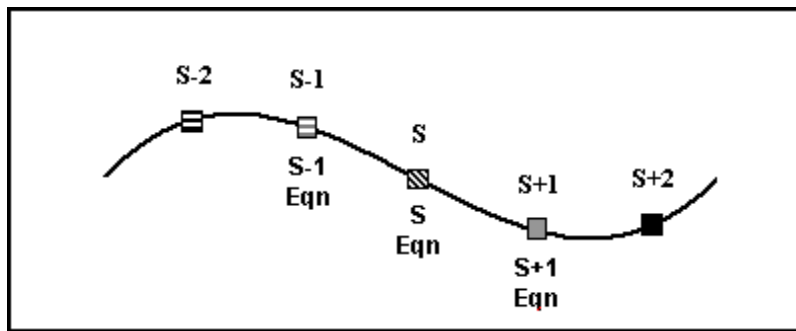


Figure 4. Example elevation profile for cubic spline interpolation.

Three equations result after expressions similar to Equation (1) are formed for the two neighboring interior points. If one assumes that the second derivatives at the end points are zero (the so-called natural cubic spline assumption), three unknowns remain in the set of three equations, representing the interior point second derivatives for the five-point series with direction θ . The three equations are then solved by Gaussian elimination for $E''_{S,\theta}$. Solutions for $E_{S-1,\theta}$ and $E_{S+1,\theta}$ are not required and are not saved. Direction θ is then incremented to its next value, and the process begins again. For window sizes of 9x9 and higher, the maximum absolute value of the cubic-spline-derived Laplacian is saved from the set of eight directional computations for the central grid cell.

The IDL programming environment provided a convenient platform and user interface for algorithm development, layer creation and image display. As developed, the algorithms process the data in two separate batch processes. The first process (BATCH_DERIV) queries the user for DEM subset boundaries and computation window size, forms the cubic spline matrix equations, finds the Laplacian by Gaussian elimination for each direction, and calculates the maximum absolute Laplacian values for each grid cell, along with their associated directions. The second process (BATCH_OVERLAY) contains procedures to calculate and plot histograms for the first and last return DSMs, bare-earth DTM, and elevation difference grid, query the user for lower and upper Laplacian and elevation difference thresholds, and calculate and display color layers from the application of thresholds to the elevation difference and Laplacian layers. A Laplacian color-coded direction layer was also created. Elevation statistics were calculated, including the minimum, maximum, mean, and standard deviation for elevation, elevation difference, slope, and Laplacian (Table 2). Values for slope and Laplacian in Table 2 are derived from absolute values.

Table 2. DSM, Elevation Difference, Bare-Earth DTM, Slope, and Laplacian Statistics

Matrix Type	min	max	mean	std. dev.
First return DSM, m	2421.11	2557.32	2542.44	30.85
Last return DSM, m	2421.10	2555.74	2542.36	30.84
Elevation difference, m	-18.64	44.54	0.12	1.22
Bare-earth DTM, m	2422.61	2555.63	2476.56	30.95
Slope (degrees)	0.00	85.43	11.84	9.04
Laplacian , /m	0.00	1.01	0.04	0.05

Processing runs were conducted to determine the optimum window size for Laplacian calculations in the creation of micro-terrain layers. The goal was to choose a window size from Table 1 that graphically identified breaklines as individual features for display without sacrificing detail within each feature. Optimum thresholds for the upper and lower values of Laplacian and elevation difference were also chosen to best represent both the micro-terrain features and canopy extent. For both the micro-terrain and canopy layers, upper thresholds were chosen to be equal to the maximum values present. However, the user may choose an upper threshold value lower than the maximum in order to examine layers representing a “slice” of the available threshold range.

Route Analysis

Open-road route analysis in ArcGIS was processed with and without the micro-terrain feature layer to assess the utility of this data with respect to cross-country mobility. Derived routes are the result of a least-cost path analysis between user-defined origin and destination points with the various terrain layers weighted based on an analysis of the effect or cost that each layer has on mobility. River channel, stream, buildings, and vegetation raster layers, all derived from the LIDAR DSM grids, were weighted as completely (100%) impassible. Both slope and micro-terrain raster layers were derived from the LIDAR bare-earth DTM. Micro-terrain features were weighted as impassible and slope was weighted according to the schema in Table 3. Typical slope along the derived routes generally did not exceed 20 degrees.

A bridge over the north-south flowing river channel in the eastern portion of the study area and another over the north-south flowing stream to the west allows for traverse across these features. Improved and unimproved roads were also delineated and assigned a weight of 0% as they help rather than hinder mobility.

Routes were delineated by contiguous 1 m GSD pixels which were converted to vector feature layers for attribution and symbolization (Figure 5). Route distance is easily determined as a feature attribute and transit time is found by querying the least-cost path analysis layer at the destination point. From route distance and transit time, average route speed is also easily derived.

Terrain Profile Extraction

To verify the identification of breaklines by the numerical methods used, the open source software package MicroDEM, developed by Dr. Peter Guth, Department of Oceanography, U.S. Naval Academy, was used for the extraction of elevation profiles of selected micro-terrain features for comparison to the spatial patterns of the extracted features. In this process, selected features from the micro-terrain layer were identified in the MicroDEM display of the bare-earth DTM. MicroDEM allows user interaction to draw a line across an elevation model display from which a vertical terrain profile is derived. These profiles were examined for locations of breaks-in-slope which were then compared to the spatial patterns of associated micro-terrain features depicted in the ArcGIS layer. Since the micro-terrain features layer shows areas of breaks-in-slope identified by the numerical model, these areas should correlate with extracted terrain profiles.

Table 3. Slope Weights

<i>Slope (deg.)</i>	<i>Weight (%)</i>						
0 – 3	0	17 – 18	36	28 – 29	58	39 – 40	80
3 – 5	5	18 – 19	38	29 – 30	60	40 – 41	82
5 – 7	10	19 – 20	40	30 – 31	62	41 – 42	84
7 – 10	20	20 – 21	42	31 – 32	64	42 – 43	86
10 – 11	22	21 – 22	44	32 – 33	66	43 – 44	88
11 – 12	24	22 – 23	46	33 – 34	68	44 – 45	90
12 – 13	26	23 – 24	48	34 – 35	70	45 – 46	92
13 – 14	28	24 – 25	50	35 – 36	72	46 – 47	94
14 – 15	30	25 – 26	52	36 – 37	74	47 – 48	96
15 – 16	32	26 – 27	54	37 – 38	76	48 – 49	98
16 – 17	34	27 – 28	56	38 – 39	78	49 – 86	100

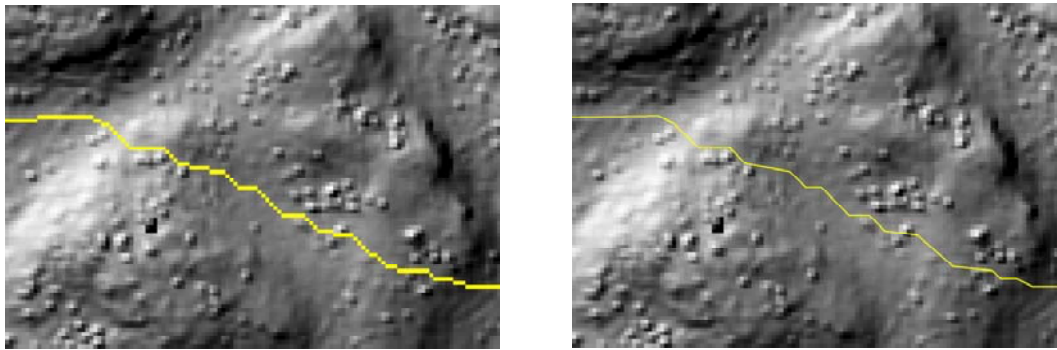


Figure 5. Raster route (left) and converted vector route (right).

RESULTS AND DISCUSSION

In this study, we extracted micro-terrain features from gridded LIDAR data as expressed by sharp breaklines, along with canopy and other feature layers, for input into a GIS environment for terrain analysis. Processing was performed in ENVI IDL, ArcGIS, and MicroDEM. After the Laplacian solution was performed and saved for the LIDAR bare-earth DTM, an elevation difference grid was computed from the first and last return DSMs for canopy extraction.

A lower threshold for the maximum Laplacian layer of 0.090/m and a kernel window size of 17x17 were chosen for the best graphical representation of micro-terrain features while retaining sufficient spatial detail. The final micro-terrain layer, combined with the thresholded canopy layer as output from IDL is shown in Figure 6 against a first return shaded relief DSM image.

The direction layer for maximum slope change, or Laplacian, was color-mapped according to one of the eight direction bins assigned to each grid cell that appears in the micro-terrain feature layer. Dominant directions across breaklines are thus associated with extracted micro-terrain features (Figure 7). When one or more breaklines that identify a particular feature have little or no directional variation, the feature will have a dominant color in the direction layer. Spatially correlated directions for groups of micro-terrain features may be useful for geologic trend analysis for fault scarps or outcropping patterns of resistant beds. The direction layer may also have application in depicting artificial modifications with breakline trends such as ditches or channels. A histogram of the set of eight calculated micro-terrain cell directions is shown in Figure 8. A bimodal distribution is evident, with two groups of micro-terrain cells having dominant directions centered about 90/270 and 0/180 degrees. Many of the cells in each

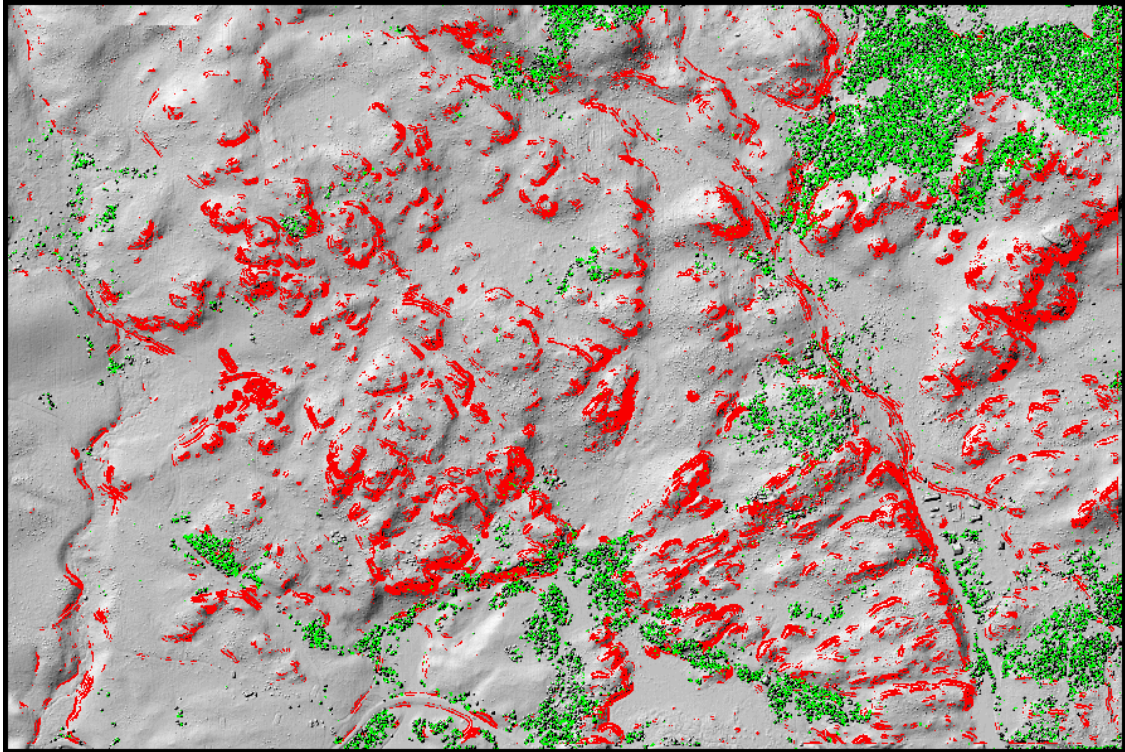


Figure 6. Micro-terrain (red) and canopy (green) over first return DSM shaded relief.

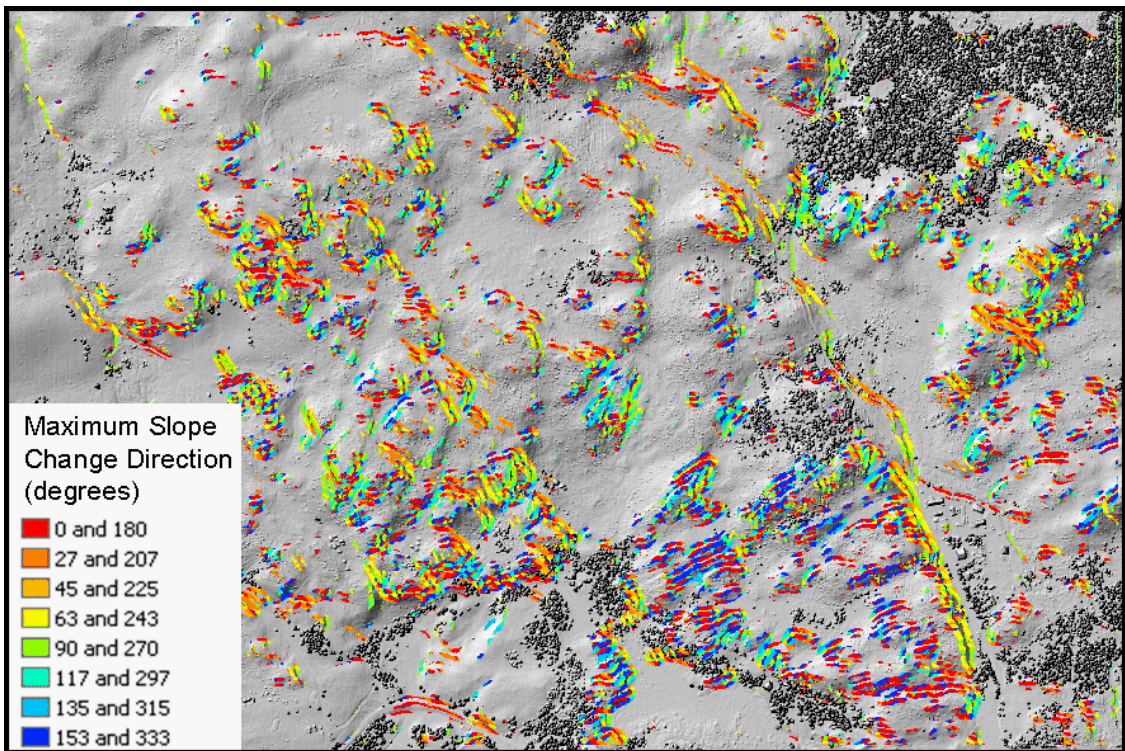


Figure 7. Micro-terrain maximum slope change directions over first return DSM shaded relief.

group are organized into features trending N-S and E-W, respectively. Figure 7 shows an area in the lower right portion of the image with dominant maximum Laplacian directions in the first and second quadrants of 0, 27, and 153 degrees, indicating a region of outcrop features belonging to the second group and trending generally E-W. This region is depicted in Figure 9, in which the direction bin colors have been re-mapped with those from Figure 8 to show E-W trending features (blue) as spatially distinct from N-S trending features with directions 63, 90, and 117 degrees (yellow). Extracted micro-terrain cells with directions of 0, 27, and 153 make up 53% of the micro-terrain cells in the entire study site; those with directions of 63, 90 and 117 degrees comprise 37%.

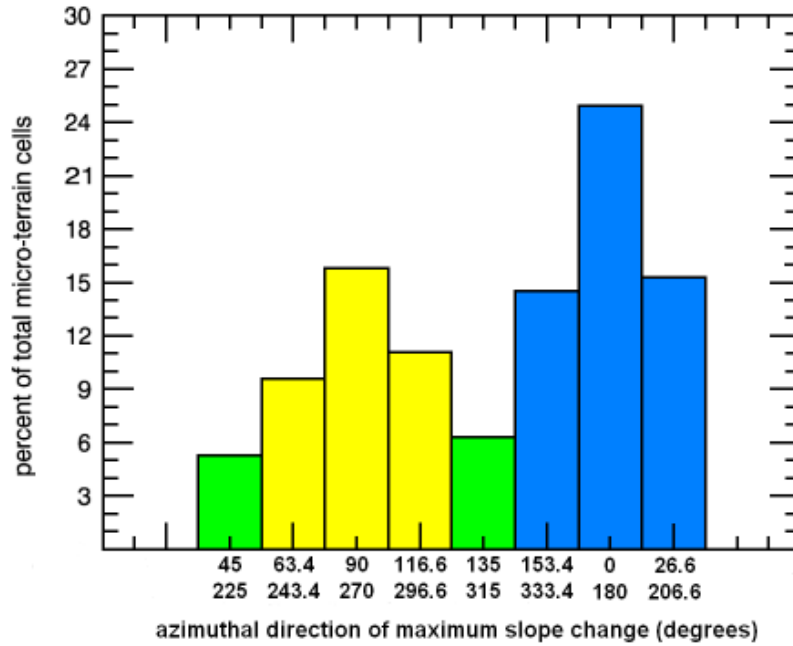


Figure 8. Distribution of maximum Laplacian cell directions.

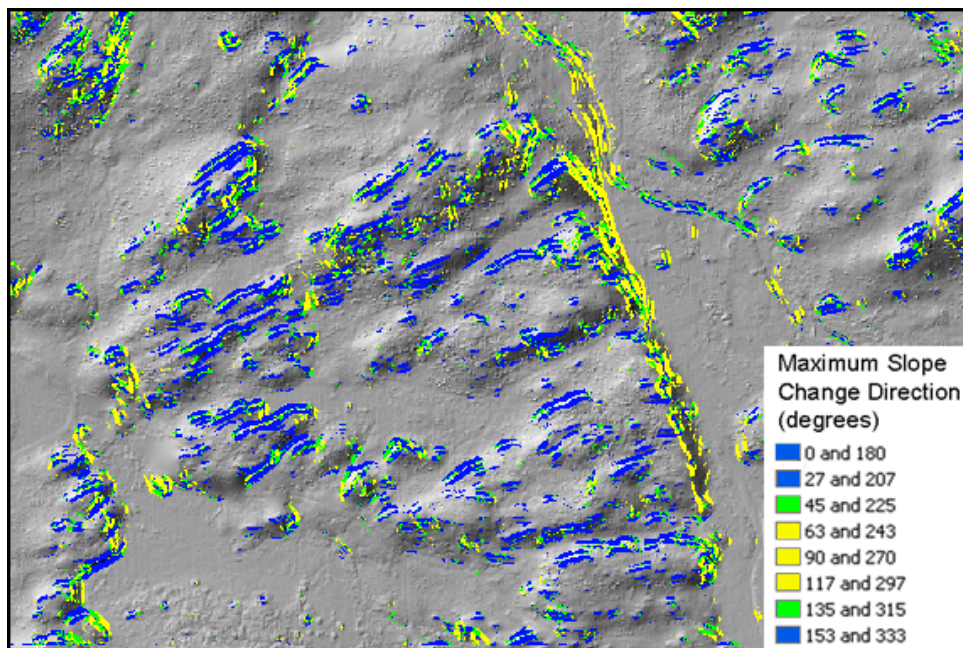


Figure 9. Subset of direction layer showing feature trending over bare-earth DTM.

Visual examination of terrain elevation profiles representing vertical cross-sections of individual micro-terrain features demonstrated correlation of breaklines with grid cell patterns of above-threshold Laplacian values. Figure 10 shows an example of a single feature from the micro-terrain layer with the trace of an extracted cross-section profile (green line). The profile shows a 6-meter high escarpment with lower and upper breaklines approximately 10 meters apart bounding a region of constant slope. The breaklines correlate with the two parallel red regions in the micro-terrain layer. The part of the profile between the breaklines where the change in slope is below the Laplacian threshold corresponds to the non-red strip between the lower and upper breaklines in the micro-terrain layer.

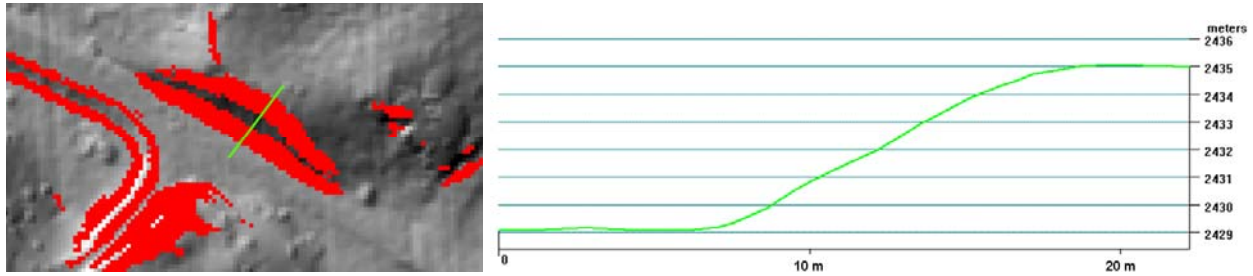


Figure 10. Micro-terrain feature and cross-section (left) and cross-section profile (right).

The off-road routing analysis shows that traversable gaps are found between impassable micro-terrain features as well as the canopy; however the micro-terrain features do impede and alter the route as expected. Figure 11 shows routes generated with and without the micro-terrain features included in the least-cost path calculation.

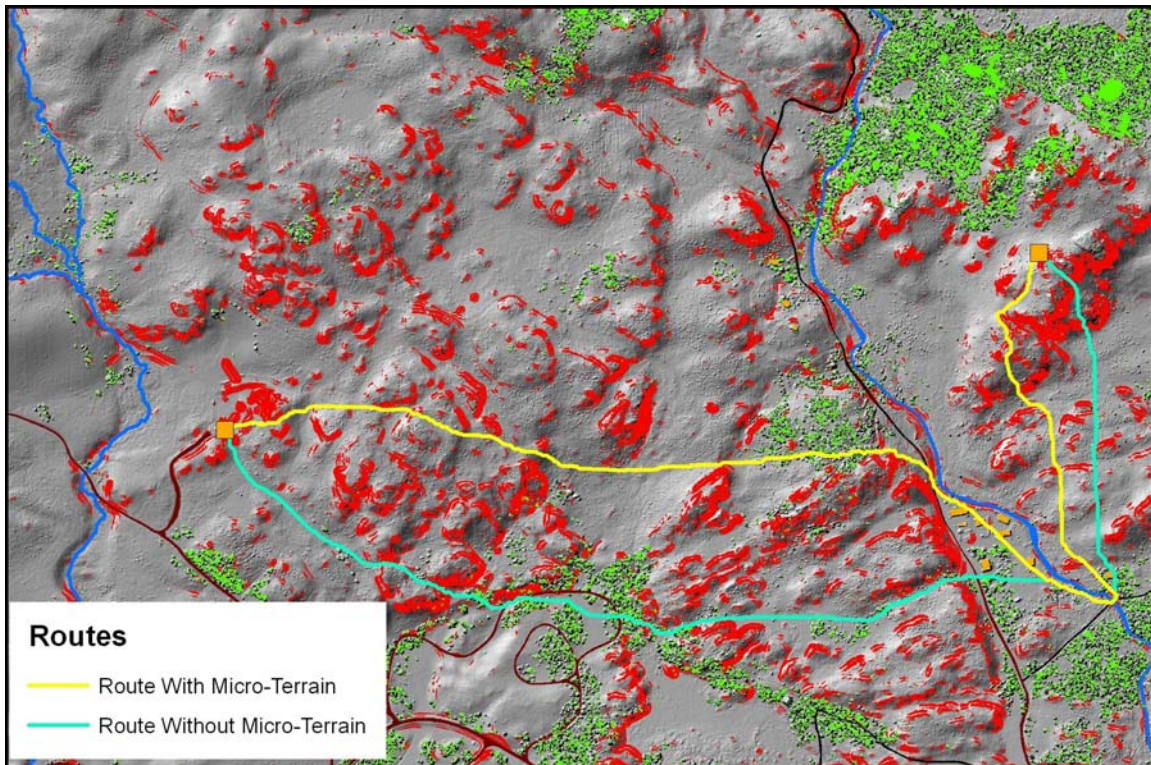


Figure 11. Effect of micro-terrain features on calculated least-cost routes.

In Figure 11, hydrology (blue), improved roads (maroon), unimproved roads (black), and buildings (orange) are also delineated. Both routes were forced to cross a bridge located in the lower right due to the impassable river feature. Although the route generated using the micro-terrain features is noticeably altered relative to that generated

without micro-terrain, the distance traveled and average speed is not markedly different. Distance with micro-terrain is 2.38 km versus 2.34 km without. Average speed with micro-terrain is 39.40 km per hour versus 40.46 km per hour without. (Maximum speed was designated as 48 km per hour.)

In terms of off-road routing, the ArcGIS least-cost path routine results are overly optimistic when both using and omitting micro-terrain features in the routine. The lack of distance and average speed disparity is in part explained by the short distance traversed as well as the least-cost path routine's efficiency in finding gaps through and between otherwise impassable features (micro-terrain and canopy). Calculated average speed is also overly optimistic in that it does not take into account the driver's caution in approaching these features and the time taken to determine alternate routes.

Whereas a typical off-road route finding routine would delineate the southerly route, inclusion of the micro-terrain features is more indicative of the real-world obstacles a driver might encounter. Micro-terrain features may thus prove to be highly valuable in route planning and in refining mobility models of vehicle as well as foot patrols. Future work in this area may include the characterization/classification of derived micro-terrain features in the field from a vehicle approach point-of-view.

SUMMARY AND CONCLUSIONS

Small-footprint airborne LIDAR systems have proven effective for terrain modeling and analysis, and can detect terrain discontinuities in non-canopy areas in spite of the undersampled nature of the pulse scanning pattern. In this work we investigated the utility of these systems for identifying and extracting micro-terrain features characterized by breaks-in-slope over short horizontal distances using numerical methods. By applying cubic spline expressions to short sequences of DTM grid cells, we created micro-terrain feature layers showing grid cells with Laplacian values above a given threshold.

Extracted elevation profiles matched the spatial distribution of identified breaklines in the micro-terrain feature layer. The profiles confirm that abrupt changes in slope are encountered at the base and the peak of the terrain cross-sections where the micro-terrain features are delineated. Another layer with color-mapped directions associated with maximum Laplacian values showed spatially correlated outcrop breakline trends in the test site DTM. This technique may be useful in trend analysis for both natural and artificial surface features identified by micro-terrain extraction.

An off-road route analysis in ArcGIS showed that the influence of micro-terrain features as route blockers significantly affected the path chosen between two points when the effects of other feature layers such as canopy, surface water, and weighted slope were held constant. Route-finding models incorporating micro-terrain features as obstacles may be more realistic for motorized and non-motorized military mobility or off-road emergency and search-and-rescue operations.

ACKNOWLEDGEMENTS

The authors wish to thank the U.S. Army Geospatial Center (AGC) Imagery Office for providing the LIDAR data for this effort. Mr. Charles Sell, U.S. Army ERDC Topographic Engineering Center, provided graphic support.

REFERENCES

- Blundell, S.B., V. Guthrie, and E. Simental, 2004. Terrain gap identification and analysis from lidar data for military mobility, *Proceedings of the American Society for Photogrammetry and Remote Sensing (ASPRS) Fall Conference, Kansas City, Missouri, September 2004*.
- Blundell, S.B., 2006. Laplacian analysis and return differencing of lidar data for improved canopy extraction, *Proceedings of the American Society for Photogrammetry and Remote Sensing (ASPRS) Fall Conference, San Antonio, Texas, November 2006*.
- Carter, W.E., R.L. Shrestha, and K.C. Slatton, 2007. Geodetic laser scanning, *Physics Today*, December 2007.
- Chapra, S.C. and R.P. Canale, 2002. *Numerical Methods for Engineers: with Software and Programming Applications, Fourth Edition*. McGraw-Hill Companies, New York, pp. 501-505.

- Chen, Q., 2007. Airborne lidar data processing and information extraction, *Photogrammetric Engineering and Remote Sensing* 73(2):109-112.
- DeBlander, L.T., 2001. *Forest Resources of the Gallatin National Forest*. U.S. Department of Agriculture, Forest Service, Rocky Mountain Research Station, June 2001.
- Dubayah, R.O., and J.B. Drake, 2000. Lidar remote sensing for forestry applications, *Journal of Forestry* 98(6):44-46.
- Engelkemeir, R.M., and S.D. Khan, 2008. Lidar mapping of faults in Houston, Texas, USA, *Geosphere* 4(1):170-182.
- Fowler, R., 2001. Topographic lidar. In *Digital Elevation Model Technologies and Applications: The DEM Users Manual*. American Society for Photogrammetry and Remote Sensing, Bethesda, MD-USA, pp. 207-236.
- Fritz, W.J., 1994. *Roadside Geology of the Yellowstone Country*. Mountain Press Publishing Company, Missoula, Montana.
- Hu, Y., and C.V. Tao, 2004. Hierarchical recovery of digital terrain models from single and multiple returns lidar data, *Proceedings of the American Society for Photogrammetry and Remote Sensing (ASPRS) Annual Conference, Denver, Colorado, May 2004*.
- Johnson, S.Y., A.R. Nelson, S.F. Personius, R.E. Wells, H.M. Kelsey, B.L. Sherrod, K. Okumura, R. Koehler III, R.C. Witter, L. Bradley, and D.J. Harding, 2004. Evidence for late Holocene earthquakes on the Utsalady Point fault, northern Puget lowland, Washington, *Bulletin of the Seismological Society of America* 94(6):2299-2316.
- Lee, I., 2004. A feature-based approach to automatic extraction of ground points for DTM generation from LIDAR data, *Proceedings of the American Society for Photogrammetry and Remote Sensing (ASPRS) Annual Conference, Denver, Colorado, May 2004*.
- Miller, S.N., S.R. Shrestha, and D. Semmens, 2004. Semi-automated extraction and validation of channel morphology from LIDAR and IFSAR terrain data, *Proceedings of the American Society for Photogrammetry and Remote Sensing (ASPRS) Annual Conference, Denver, Colorado, May 2004*.
- Mitasova, H., M.Overton, and R.S. Harmon, 2005. Geospatial analysis of a coastal sand dune field evolution: Jockey's Ridge, North Carolina, *Geomorphology* 72:204-221.
- Priestnall, G., J. Jaafar, and A. Duncan, 2000. Extracting urban features from LiDAR digital surface models, *Computers, Environment, and Urban Systems* 24:65-78.
- Watt, P.J., and D.N.M. Donoghue, 2005. Measuring forest structure with terrestrial laser scanning, *International Journal of Remote Sensing* 26(7):1437-1446.
- Woolard, J.W. and J.D. Colby, 2002. Spatial characterization, spatial resolution, and volumetric change of coastal dunes using airborne LIDAR: Cape Hatteras, North Carolina, *Geomorphology* 48:269-287.